applied sciences

Article

# Theoretical and Experimental Investigations on the Ultra-Low-Frequency Broadband of Quasi-Static Metamaterials

**Haixia Liu [1], Weitao He [1], Lixia Li [1,2,*] and Qi Jia [1]**

[1] School of Mechanical and Electrical Engineering, Xi'an University of Architecture and Technology, Xi'an 710055, China
[2] Institute of Mechanics, Xi'an University of Architecture and Technology, Xi'an 710055, China
* Correspondence: lilixia@xauat.edu.cn

**Abstract:** This paper proposes an I-shaped radial elastic metamaterial with ultra-low-frequency broadband characteristics and studies the propagation characteristics of elastic waves in their quasi-static state. Through the calculation of the dispersion relationship, the frequency response function, and the eigenmode displacement field, it is found that the ultra-low-frequency wide band gap can be generated in the quasi-static metamaterial. The wide band gap is mainly caused by modal transitions. The equivalent mass–spring model reveals the modal changes of the I-shaped radial elastic metamaterial under the surface constraints. Furthermore, by studying the directional vibration displacement field of the finite period structure, it is demonstrated that the mechanism of the ultra-low-frequency broadband ($0 < Reduced\ frequency(\Omega) < 0.20$) is the local resonance mechanism. Subsequently, the influence of the geometric and the material parameters on the location and width of the band gap is explored numerically. Finally, based on the model, through the hammer modal experiment, it is proven that the quasi-static structure yields an ultra-low-frequency stop band of 0.1–1012 Hz. The research conclusions can be applied to mechanical engineering fields such as ultra-low-frequency vibration reduction.

**Keywords:** elastic metamaterial; local resonance; finite element method; vibration control

**Citation:** Liu, H.; He, W.; Li, L.; Jia, Q. Theoretical and Experimental Investigations on the Ultra-Low-Frequency Broadband of Quasi-Static Metamaterials. *Appl. Sci.* **2022**, *12*, 8981. https://doi.org/10.3390/app12188981

Academic Editor: Dimitrios Zografopoulos

Received: 3 August 2022
Accepted: 5 September 2022
Published: 7 September 2022

## 1. Introduction

Phononic crystals [1,2] are periodic structures that can control elastic waves in solids. Due to their excellent band gap properties, phononic crystals are widely investigated. The existing band gap formation mechanisms in phononic crystals are mainly the Bragg scattering mechanism [3–5] and the local resonance mechanism [6]. For the phononic crystals based on the Bragg scattering mechanism, the generation of the band gap results from the interaction between the periodically changing material properties and elastic waves. The scale of the scatterer and the wavelength corresponding to the band gap frequency are in the same order of magnitude. Therefore, a large space size is required to block the vibration [5]. With the excitation of the elastic waves in the phononic crystal based on the local resonance mechanism [7], the scatterer oscillator resonates and interacts with the elastic wave. Furthermore, the band gap frequency is much lower than that of the Bragg band gap of the same lattice size, enabling a small size to control large wavelengths.

Phononic crystals dominated by local resonance mechanisms are also called elastic metamaterials [8–10]. To facilitate the application of elastic metamaterials in vibration control and mechanical engineering, it is essential to obtain low-frequency and large-bandwidth band gaps. Researchers have put a substantial amount of effort in elastic metamaterials with planar periodic arrangement to explore metamaterial structures with excellent band gap properties [11–13]. Badreddine Assouar et al. [14] designed an elastic metamaterial with double-sided short cylinders periodically arranged in the X and Y directions and obtained a broadband full band gap calculated by the finite element method.

A.O. Krushynsk et al. [15] investigated an elastic metamaterial with a rubber coating. They obtained a low-frequency band gap, with an initial frequency below 200 Hz, by arranging the lattice structure periodically in a plane. Gao et al. [16] proposed a two-dimensional elastic metamaterial with the periodic distribution of dual resonators in the X and Y directions, which generated a 5 Hz wide ultra-low-frequency band gap around 35 Hz.

Radial elastic metamaterials (REMs) [17–26] are annular structures arranged periodically in the radial direction with omnidirectional band gap properties. Shi et al. [23] proposed an REM composed of alternating plexiglass and steel materials to obtain a broadband complete band gap. Ma et al. [25] investigated double-layer REMs with lattice slip properties, and their structures exhibited broadband band gap properties. Li et al. [20] designed a substrate composed of alternating aluminum and epoxy resin-based structure, added periodic rubber and steel block REMs on the substrate, and obtained a band gap with an initial frequency below 500 Hz and a bandwidth of about 100 Hz. Gao et al. [27] designed a radial elastic metamaterial with steel as the matrix and a combined mass of silicone rubber and steel. The center frequency of the first-order band gap was found to exist around 300 Hz. Although the radial elastic metamaterials aim to achieve low-frequency stop bands, it is still difficult to achieve ultra-low-frequency stop bands.

Some researchers [21–24] found that the quasi-static periodic structure can open a wide-band stop band in the ultra-low-frequency range. Yao et al. [28] designed a special mass–spring system. They showed that the quasi-static system effectively attenuated the elastic waves in the ultra-low-frequency range by fixing the external boundary of the model. T. Antonakakis et al. [22] investigated the shielding phenomenon of the flexural waves in quasi-static elastic plates by imposing fixed constraints on special points on the elastic plate. They found out that the form of point confinement caused the structure to produce ultra-low stop bands. Through the Fourier series and high frequency homogenization theory, T. Antonakakis et al. [29] investigated the cause of the zero-frequency initial stop band from the mathematical point of view. Y Achaoui et al. [30] designed a broadband quasi-static two-dimensional seismic metamaterial with a zero-frequency initial stop band. They imposed constraints on the bottom surface of its periodic structure, which effectively attenuated the seismic waves.

The above studies have demonstrated the feasibility of the ultra-low-frequency band theoretically. However, these studies have not achieved ultra-wide low-frequency bands, and their mechanisms and experiments have not been analyzed in detail. Moreover, the above quasi-static band gap studies are based on the periodic structure in the Cartesian coordinate system, but no relevant research has been carried out on the radial periodic structure.

In this study, we propose an I-shaped single-phase REM and investigate its quasi-static band gap properties. The eigenmode visualization method is used to analyze the generation mechanism of the ultra-low-frequency broadband. Furthermore, the influence of the structural parameters on the location and bandwidth of the ultra-low-frequency broadband is analyzed. Finally, the existence of the ultra-low-frequency broadband is verified experimentally. The quasi-static REMs are proposed to realize ultra-low-frequency broadband, which has important practical significance for engineering applications such as ultra-low-frequency vibration reduction in metamaterial structures.

## 2. Models and the Theoretical Methods

### 2.1. Quasi-Static REM Structure

Figure 1a shows the unit lattice structure of the proposed I-shaped REM. Here, $a$ denotes the leg width of the I-shaped unit lattice structure, i.e., the lattice constant, whereas $h$, $d$, and $e$ denote the waist height, waist thickness, and average leg thickness of the I-shaped unit lattice structure, respectively. The radial periodic arrangement of the unit lattice to form metamaterials is shown in Figure 1b. Figure 1c imposes surface constraints on the Z-direction basal plane (blue represents the constrained surface of the metamaterial structure), thereby constructing a quasi-static metamaterial [31].

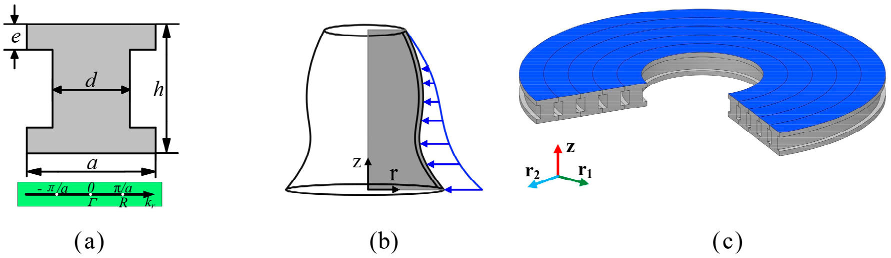

**Figure 1.** REM: (**a**) Schematic diagram of REM lattice structure and BZ wave vector (Gamma-R) in reciprocal space. (**b**) Formation of REM. (**c**) Quasi-static supermaterial.

### *2.2. Theoretical Method*

In order to study the band gap characteristics of the metamaterial structures, according to the theory of elastic dynamics, the elastic wave equation with displacement as the unknown quantity in the Cartesian coordinate system is established. With the assumptions of material continuity, complete elasticity, homogeneity, isotropy, and small deformations [30], the elastic wave equation is expressed as:

$$\rho \frac{\partial^2 u_i}{\partial t^2} = \sum_{j=1}^{3} \left\{ \frac{\partial}{\partial x_i} \left( \lambda \frac{\partial u_j}{\partial u_j} \right) + \frac{\partial}{\partial x_j} \left[ \mu \left( \frac{\partial u_i}{\partial x_j} + \frac{\partial u_j}{\partial x_i} \right) \right] \right\} + \rho f_i \tag{1}$$

where $u_i$ and $u_j$ denote the displacement components, $f_i$ denotes the external force per unit volume, $\rho$ denotes the density, $t$ denotes the time, and $\lambda$ and $\mu$ denote the Lame elastic constants of the material.

For the particularity of the structure, we establish the elastic wave equation in the cylindrical coordinate system to calculate the dispersion relation curve in the infinite system based on the equations of motion, geometry, and physics. Here, $u$, $v$, and $\omega$ denote the displacement components of the cylindrical coordinate system and $r$, $\theta$, and $z$ denote the coordinate components in the cylindrical coordinate system.

$$\begin{cases} \rho \frac{\partial^2 u}{\partial t^2} = (\lambda + 2\mu) \frac{\partial \theta_t}{\partial r} - \frac{2\mu}{r} \frac{\partial w'_z}{\partial \theta} + 2\mu \frac{\partial w'_\theta}{\partial z} + \rho f_i \\ \rho \frac{\partial^2 v}{\partial t^2} = (\lambda + 2\mu) \frac{\partial \theta_t}{r \partial \theta} - 2\mu \frac{\partial w'_z}{\partial z} + 2\mu \frac{\partial w'_r}{\partial r} + \rho f_i \\ \rho \frac{\partial^2 w}{\partial t^2} = (\lambda + 2\mu) \frac{\partial \theta_t}{\partial z} - \frac{2\mu}{r} \frac{\partial}{\partial r} \left( r w'_\theta \right) + \frac{2\mu}{r} \frac{\partial w'_r}{\partial \theta} + \rho f_i \end{cases} \tag{2}$$

where the volume strain $\theta_t$ and rotational components ($w'_r$,$w'_\theta$, $w'_z$) are defined as:

$$\begin{cases} \theta_t = \frac{1}{r} \frac{\partial (ru)}{\partial r} + \frac{1}{r} \frac{\partial v}{\partial \theta} \frac{\partial w}{\partial z} \\ w'_r = \frac{1}{2} \left( \frac{1}{r} \frac{\partial w}{\partial \theta} + \frac{1}{r} \frac{\partial v}{\partial z} \right) \\ w'_\theta = \frac{1}{2} \left( \frac{1}{r} \frac{\partial u}{\partial \theta} + \frac{\partial w}{\partial r} \right) \\ w'_z = \frac{1}{2} \left( \frac{1}{r} \frac{\partial (rv)}{\partial \theta} + \frac{\partial u}{\partial \theta} \right) \end{cases} \tag{3}$$

According to Bloch's theorem, only a single lattice cell needs to be considered since the periodic structure of lattice cells is infinite along the radial direction. Its lattice boundary condition equation is:

$$u(r + r_a, z) = u(r, z) \mathrm{e}^{\mathrm{i} k_r r_a} \tag{4}$$

where $r$ denotes the radial position, $a$ denotes the lattice constant, and $k_r$ denotes the components of the Bloch wave vector, $K_r$, in the radial direction.

Using Equation (4), by establishing the model as shown in Figure 1a under the 2D axisymmetric of COMSOL Multiphysics, applying a periodic boundary condition on r, sweeping the Bloch wave vector over the boundary of the first irreducible ($\Gamma(0,0)$ to $R(1,0)$) Brillouin zone (IBZ), the dispersion relation curve of the radial metamaterial structure is obtained.

It is worth noting here that the quasi-static limit of the dispersion curves can be inferred from the slope or curvature of the dispersion curve around the point $\Gamma$ when $K_r \to 0$ [30,32,33]. Meanwhile, the effective behavior of the low-frequency Bloch waves can be explained by the effective group velocity or effective mass [28,34]. When some Dirichlet data $u \to 0$ (fixed state, possibly minimal existence) are set on a certain region within the IBZ, it is deduced that $u$ is 0 everywhere in the IBZ using the maximum principle [32,33]. It is indicated that the period-constrained elastic structure has an ultra-low-frequency band gap with an onset of near-zero frequency, which can be used to reflect elastic waves at any low frequency.

## 3. Ultra-Low-Frequency Broadband Characteristics

### *3.1. Ultra-Low-Frequency Broadband Structure Analysis*

In order to explore the band gap properties of the quasi-static metamaterials, the finite element method is used to calculate the dispersion relationship of the quasi-static metamaterial structure and the results are presented in Figure 2. Here, the blue solid line represents the real part of the wave vector, i.e., the wave propagation mode, and the red dotted line represents the imaginary part of the wave vector, i.e., the wave evanescent mode. It is worth noting that the absolute value of the imaginary part of the wave vector represents the attenuation of the elastic wave amplitude in the space, i.e., there is an evanescent wave mode. The metamaterial geometry parameters are given as follows: the lattice constant $a$, the waist height $h = a$, the waist thickness $d = 0.6a$, and the average leg thickness $e = 0.2a$. The material is epoxy resin, and the material parameters are: the elastic modulus $E = 4.35 \times 10^9$ Pa, Poisson's ratio $\mu = 0.368$, the mass density $\rho = 1180\ \mathrm{kg/m^3}$, the reduced frequency $\Omega = \omega a / 2\pi c_t$, and the shear wave velocity of the epoxy resin matrix $c_t = 1160.8\ \mathrm{m/s}$.

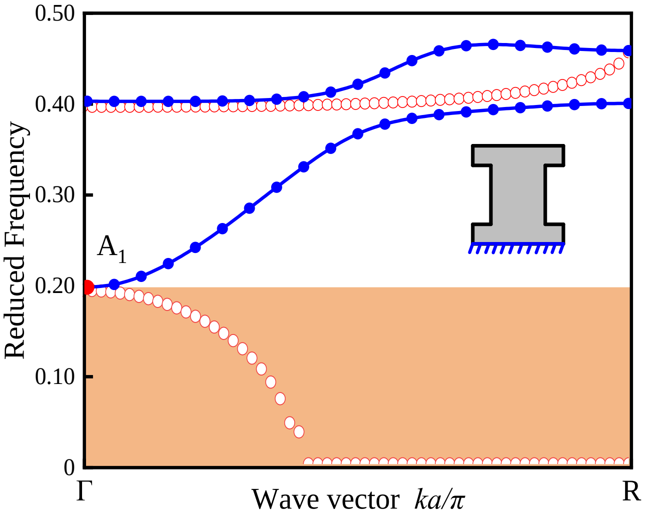

**Figure 2.** Dispersion relationship curve of the quasi-static REMs.

Figure 2 shows the dispersion relation curves of the quasi-static radial metamaterial structure. As shown in Figure 2, the ultra-low-frequency broadband appears in the quasi-static I-shaped radial elastic metamaterials. There are only two energy band curves below the parsimonious frequency $\Omega = 0.50$. Its first band gap ($0 < \Omega < 0.20$) is below the first energy band. It is worth noting that the imaginary part of the energy band has a part greater than zero in the band gap frequency range, indicating the generation of evanescent waves. Furthermore, the imaginary part of the band in the first band gap changes sharply with the frequency. This is the hallmark of a typical local resonance. Similar changes have been observed in one-dimensional metamaterials [34]. In this case, the dispersion relation is significantly different from the typical Bragg scattering band gap dispersion curve.

In order to further verify the correction of the band structure, the 5/10-period quasi-static metamaterial frequency response curves are calculated as shown in Figure 3. It can be observed that there is a good agreement between the band gap position and the band gap results obtained from the dispersion curve.

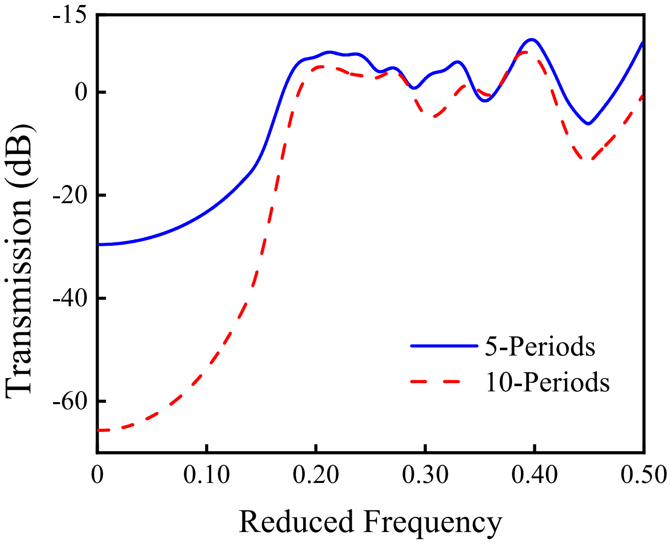

**Figure 3.** Frequency response functions of the quasi −static REM.

### 3.2. Mechanism of the Ultra-Low Broadband Characteristics

In order to research the mechanism of the ultra-low-frequency broadband, the dispersion relation curves of conventional radial metamaterials are calculated under the condition that the structure and material parameters remain unchanged, and the results are presented in Figure 4. It can be seen that there is no ultra-low-frequency broadband in the range of the parsimonious frequency $0 < \Omega < 0.50$. Figure 5 shows the calculated eigenmode displacement vector fields for the special points of the energy bands in the two states, respectively. Here, the black arrows indicate the directions of the vibration displacement and the colors indicate the magnitude of the vibration displacement.

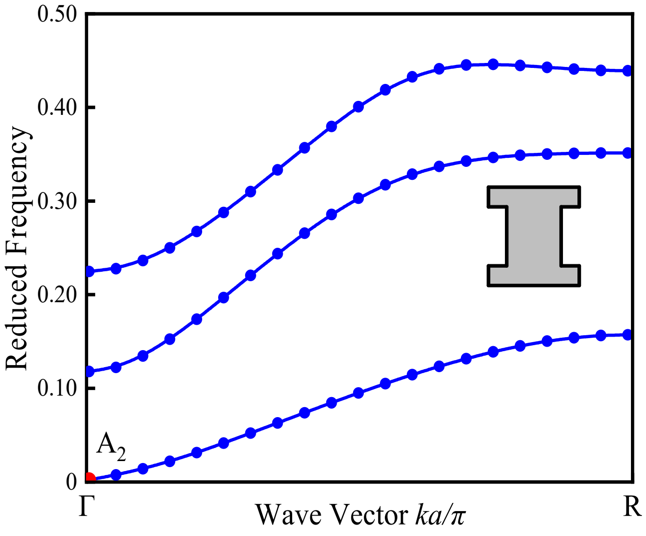

**Figure 4.** The unconstrained REM dispersion relation curve.

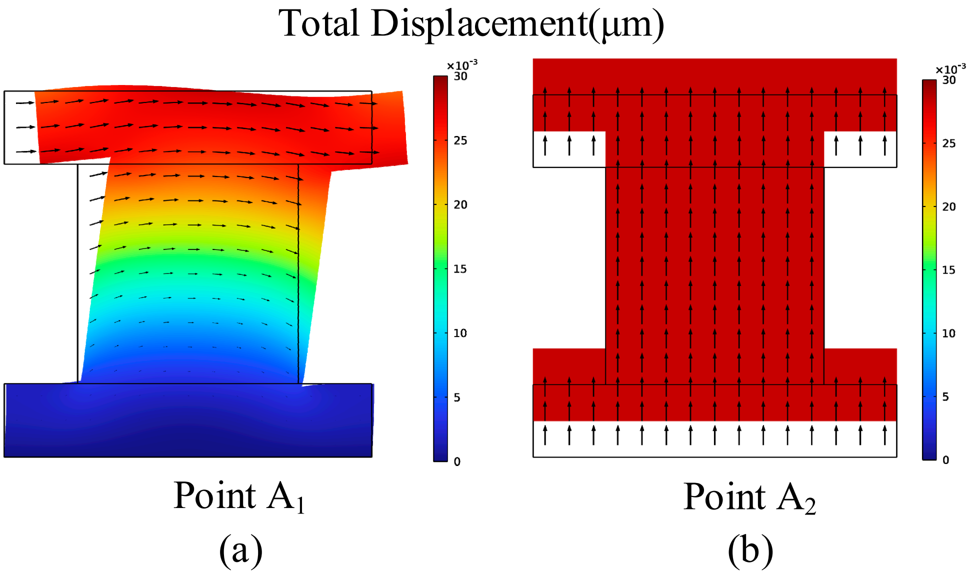

**Figure 5.** The eigenmodes and the displacement vector fields of the special points.

Referring to point $A_1$ in Figure 2, the vibration energy is concentrated at the free end of the unit cell, whereas the whole represents a localized rotational vibration mode, similar to a "pendulum". This is due to the constraints imposed by Z on the base surface so that the vibration cannot be generated at the lower base surface. At point $A_2$, since the upper and lower basal planes are free boundaries, the vibration is evenly distributed throughout the entire unit cell. This entails an overall vertical vibration mode of the axial direction. Due to the face constraints, the structural intrinsic eigenmode displacement vector field is changed, and the localized vibration of the metamaterials opens the ultra-low-frequency broadband.

Furthermore, the vibration characteristics of the finite-period metamaterial structures are studied and the generation mechanism of the ultra-low-frequency broadband characteristics of the quasi-static radial metamaterials is explored. Figure 6 shows the displacement field along the radial direction at the center frequency of the first band gap of the quasi-static radial metamaterial for ten periods. Here, the center frequency $\Omega$ of the first band gap is 0.10 in its quasi-static state. The incident wave is effectively reflected, and a localized vibration mode appears. Inside the metamaterial array, the vibration amplitude is the greatest at the first lattice. Afterwards, the amplitude decays exponentially towards the exit, where a low transmission is observed on the exit side. The vibration mode at the first lattice is symmetric along the axial direction, which is consistent with the experimental results [35]. However, in the radial displacement field outside the ten-period quasi-static radial metamaterial band gap range (at the parsimonious frequency $\Omega = 0.30$), it is observed that the incident Lamb wave passes through the metamaterial structure almost unperturbed, as shown in Figure 7. Its displacement values can reach up to 2 mm due to the superposition of the reflections. Therefore, the structural local resonance is the main reason for the attenuation of the incident Lamb wave.

According to the analysis of the above-mentioned quasi-static REM unit cell eigenmode displacement vector field and the radial vibration displacement field, the lower base surface of its local vibration mode is stationary, whereas the upper free end is equivalent to a single-degree-of-freedom system. In addition, its local resonance structure can be equivalent to a mass–spring system [35]. The cut-off frequency of its resonant band gap can be determined by the natural frequency of the local resonance, and it can be evaluated in terms of the equivalent mass (which provides the mass part) and the equivalent stiffness (which provides the elastic part) for this vibration mode:

$$f = \sqrt{(K_e/M_e)}/2\pi \tag{5}$$

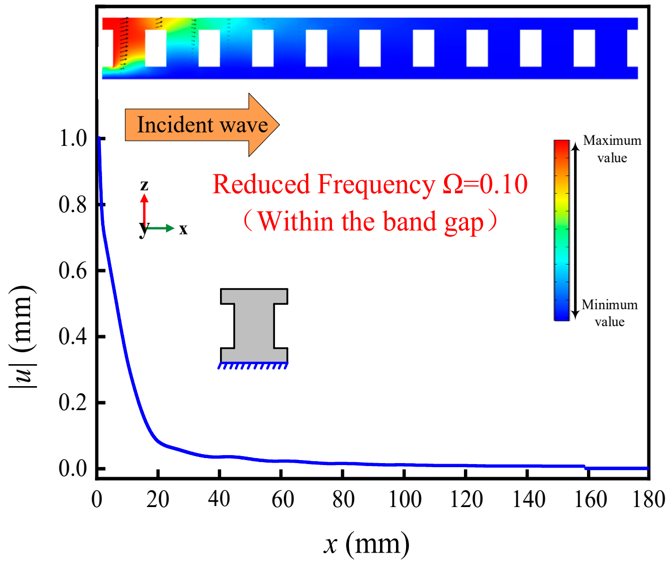

**Figure 6.** Radial vibration displacement field of the quasi-static REMs.

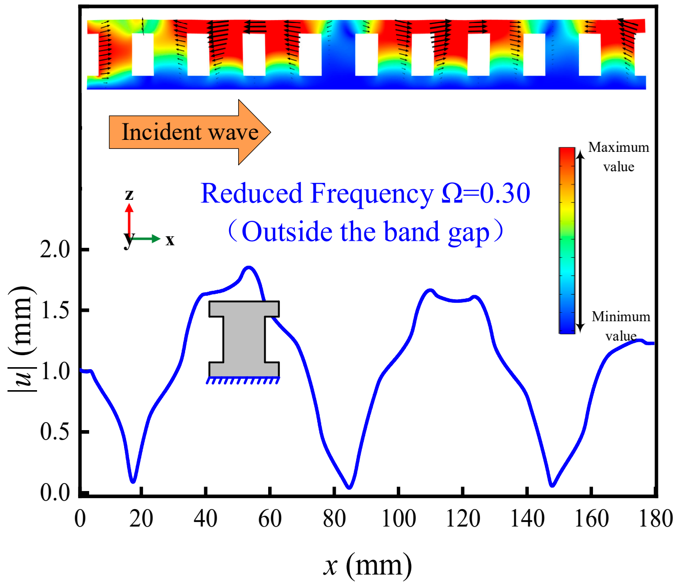

**Figure 7.** Radial vibration displacement field outside the band gap of the quasi-static REMs.

The middle part of the I-shaped structure acts as a $K_e$ providing equivalent stiffness, while the upper free end acts as an $M_e$ providing equivalent mass. The equivalent stiffness and the mass represented here are different in different modes. From Equation (5), it can be seen that changing the equivalent stiffness or mass of its corresponding part can adjust the frequency position and the width of its band gap.

### *3.3. Influence of the Geometric Parameters on the Ultra-Low-Frequency Broadband Characteristics*

To analyze the relationship between the resonant band gap frequency and the width and the structural parameters in detail, this section investigates the effect of changing the band gap properties of the aligned static metamaterials by a single geometric parameter. Figure 8a shows the variation law of the first band gap with the geometric parameter d/a ratio. The cutoff frequency in Figure 8a shows a gradually increasing trend where the band gap width increases monotonically as $d/a$ increases. As shown in Figure 8b, the middle part of the I-shaped structure acts as a spring providing equivalent stiffness, while the upper free end acts as a mass body providing equivalent mass. With the increase in the parameter $d/a$, the equivalent mass $M_e$ in the structure remains almost unchanged, and the equivalent stiffness $K_e$ keeps increasing, which is the reason for the increased cut-off frequency.

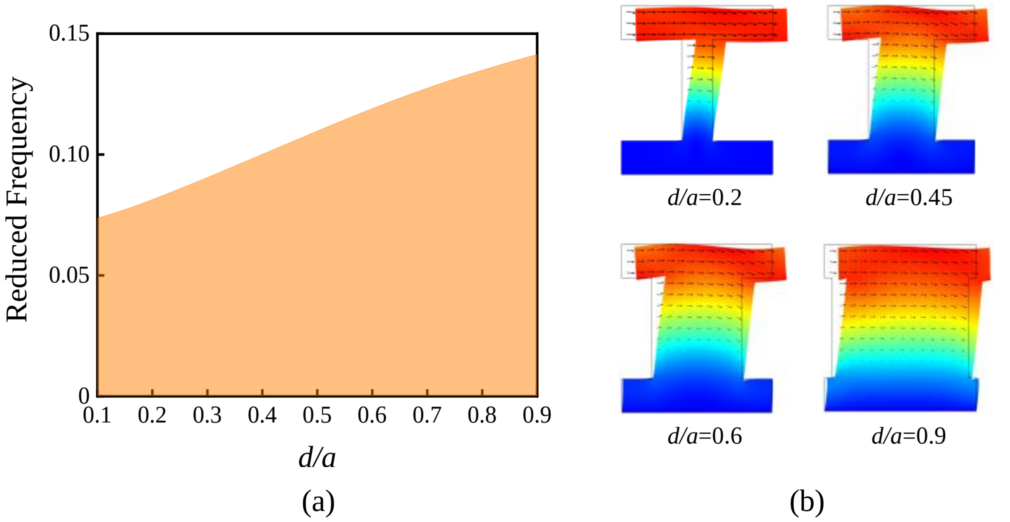

**Figure 8.** Relationship between the band gap characteristic and the parameter ratio $d/a$. (**a**) Relationship function curve and (**b**) eigenmode displacement vector field.

Figure 9a shows the variation in the band gap of the quasi-static REM with the geometric parameter ratio $e/a$. The cutoff frequency of the first band gap shows a monotonically increasing trend with the increase in $e/a$ while also affecting its band gap width, which becomes wider with the increase in $e/a$. To explore the reason for the variation in the band gap width, the eigenmode displacement vector fields for different $e/a$ values are calculated, and the results are presented in Figure 9b. The results show that with the increase in $e/a$, the torsional stiffness of the I-shaped structure increases continuously. This continuous increase in the torsional stiffness results in a weakened torsional vibration on the upper and lower sides of the structure. On the other hand, the local radial vibration of the structure is strengthened gradually. The continuous enhancement of the radial vibration coupling between the upper and the lower sides of the structure as well as the middle of the structure is the main reason for the continuous increase in the cut-off frequency and the gradual increase in the band gap width.

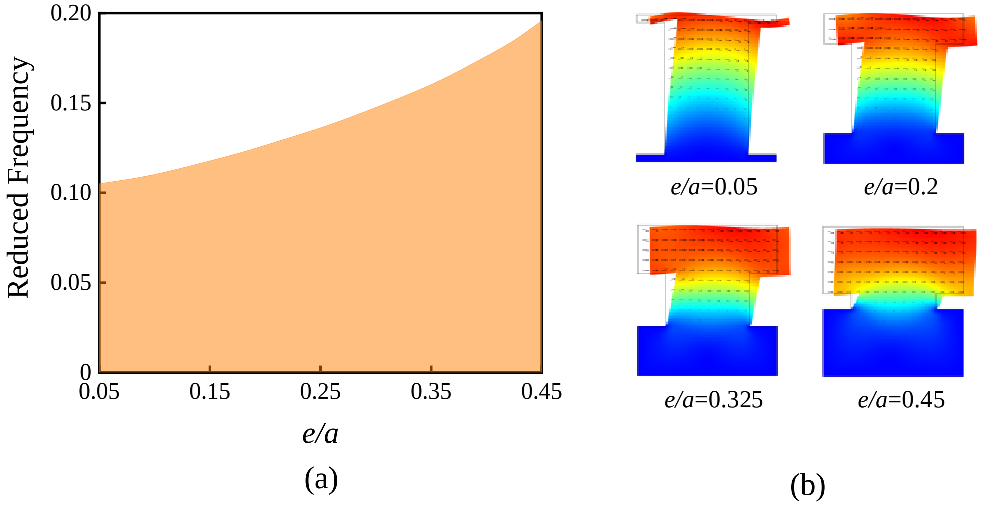

**Figure 9.** Relationship between the band gap characteristic and the parameter ratio $e/a$. (**a**) Relationship function curve and (**b**) eigenmode displacement vector field.

The results show that this is precisely due to the fixed confinement of the lower surface that the energy band transitions, which in turn opens the ultra-low-frequency band gap. Moreover, the cut-off frequency in the ultra-low-frequency band can be adjusted by the resonant frequency of the oscillator.

### *3.4. Influence of the Material Parameters on the Ultra-Low-Frequency Broadband Characteristics*

In this subsection, the effect of the structural material parameters on the band gap properties is investigated. Generally, the elastic modulus $E$ and the mass density $\rho$ of the epoxy resins are found to be within $1-10$ GPa and $800-2300$ kg/m$^3$, respectively. In this study, the elastic modulus $E$ and the mass density $\rho$ are changed while keeping the other material and geometric parameters, and the results are presented in Figure 10. The results show that as the elastic modulus of the structure increases from 1 GPa to 10 GPa, its band gap gradually increases and moves to a higher frequency direction. This is due to the increase in the structural elastic modulus, which leads to an increase in the structural stiffness. As a result, the cutoff frequency of its band gap is shifted to higher frequencies. As the mass density $\rho$ increases, the band gap narrows gradually and its center frequency goes down slowly. With the change in the mass density $\rho$ of the structure, the coupled resonance mode of the structure and the Lamb wave mode changes accordingly, which causes the resonance frequency of the structure to shift to lower frequencies.

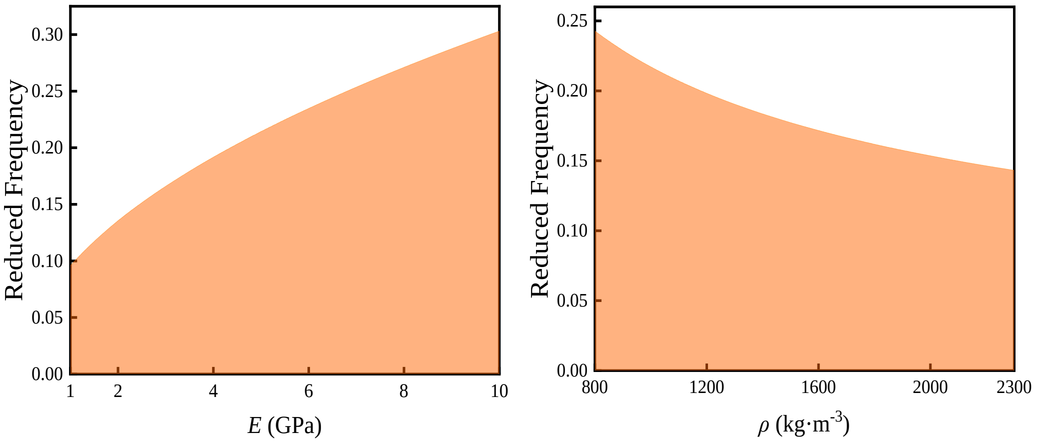

(a) (b)

**Figure 10.** Effect of the material parameters on the band gap characteristics.

## 4. Time Domain Analysis of the Ultra-Low-Frequency Broadband Characteristics

In order to further explore the attenuation characteristics of the quasi-static metamaterials for the elastic waves in the ultra-low frequency range, a three-dimensional full-scale radial metamaterial structure with finite period is designed. It contains in-plane and out-of-plane modes, as shown in Figure 11. The distance between the vibration source and the center of the quasistatic metamaterial finite periodic structure is 15a, the cross-sectional width is 19a, and its structure height h is small enough to make only Lamb waves propagate in the quasi-static metamaterial.

In addition, the finite period model of the quasi-static metamaterial used for the calculation has the same fixed bottom boundary. The tetrahedral mesh adopts the quadratic element size $\lambda_s/5$ ($\lambda_s$ is the wavelength of the surface wave), and its transient calculation time step is set to $1/60\ f_{max}$ ($f_{max}$ is the maximum expected frequency) to ensure the accuracy of the calculation results.

At point A, the oscillation source in the X direction on the free surface is used to introduce Lamb waves, and the low-reflection boundaries are set on the surrounding sides of the structure to reduce any unwanted reflections and to make the results more realistic and reliable. In this section, two different input signals are investigated. The excitation signals are modulated by the sum of 7 and 21 sinusoidal cycles with a Hanning window centered at the band gap frequency of 580 Hz. Their time-evolved Fourier spectra are shown in Figures 12b and 13b, respectively.

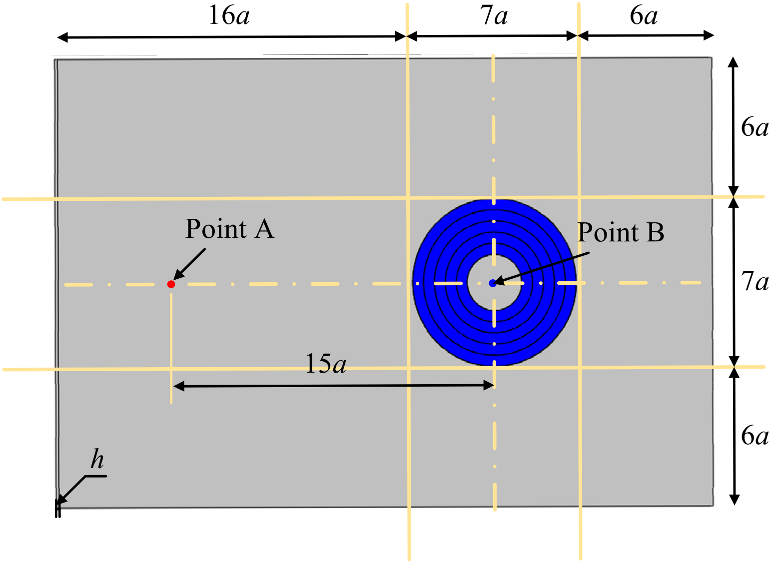

**Figure 11.** Three-dimensional full-scale finite periodic REM structure.

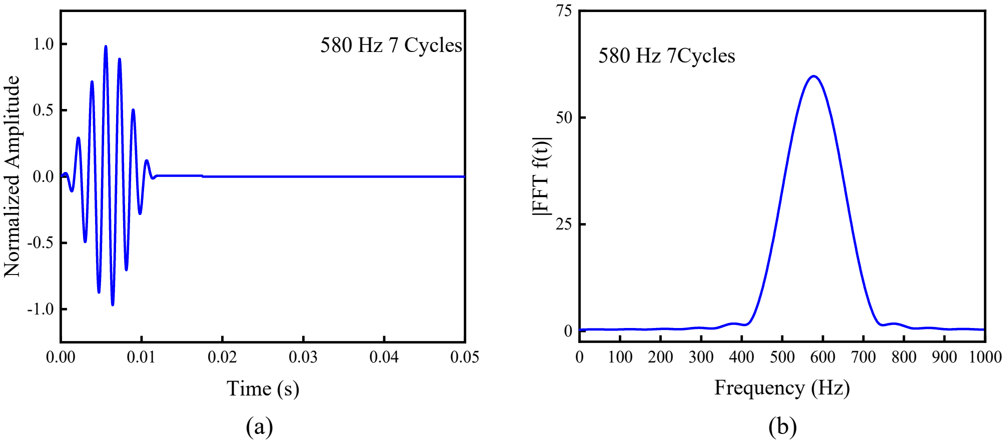

**Figure 12.** 580 Hz, 7-cycle excitation signal. (**a**) Time–history curve of the excitation signal and (**b**) frequency content of the excitation signal.

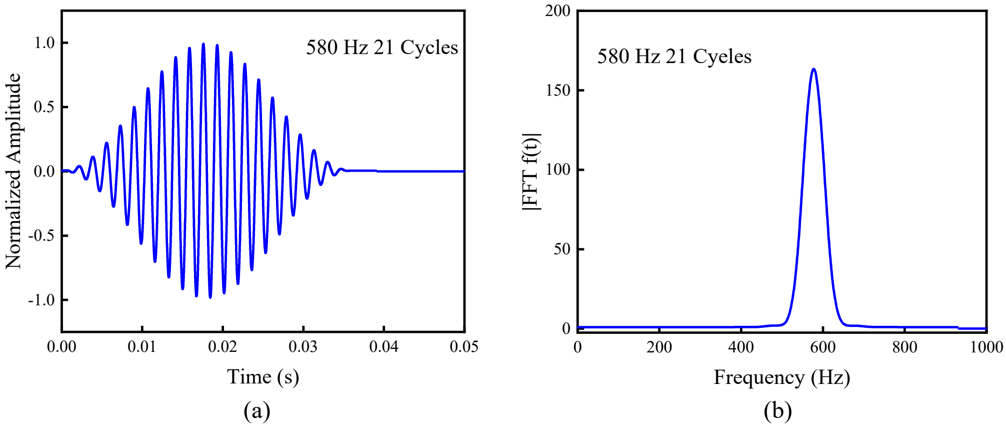

**Figure 13.** 580 Hz, 21-cycle excitation signal. (**a**) Time–history curve of excitation signal and (**b**) frequency content of excitation signal.

At point A (see Figure 10), two excited signals of 7/21 sinusoidal cycles modulated by Hanning at 580 Hz are entered. The instantaneous transient display responses of 0.05 s duration are performed respectively, ensuring that the excitation signal emitted by the emission point A can reach and pass through the quasi-static metamaterial structure. To avoid reflections from the boundary around the model, the response signals are picked up at point B, as shown in Figures 14 and 15. As shown in Figures 14a and 15a, due to the existence of the quasi-static metamaterials, the propagation of Lamb waves is effectively suppressed, and its amplitude attenuation can exceed 70% (the blue solid line represents the amplitude signal of the Lamb wave without the metamaterial, and the red dotted line represents the amplitude signal of the Lamb wave with the metamaterials). Subsequently, the Fourier transform of the response signal is performed, and its frequency contents are compared, as shown in Figures 14b and 15b.

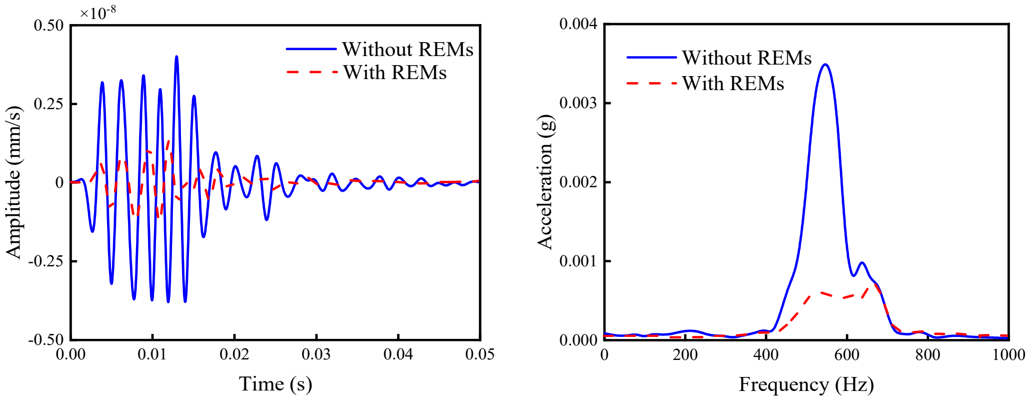

(a) (b)

**Figure 14.** 580 Hz, 21-cycle excitation signal response. (**a**) Time–history curve of response signal; (**b**) Fourier spectrum of response signal.

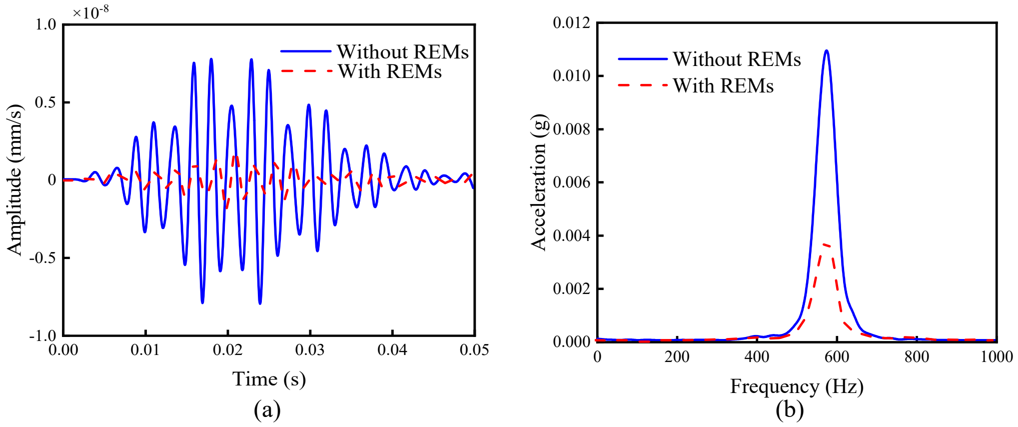

(a) (b)

**Figure 15.** 580 Hz, 21-cycle excitation signal response. (**a**) Time–history curve of response signal and (**b**) Fourier spectrum of response signal.

These results show that the quasi-static metamaterial can attenuate the Lamb waves finitely in the band gap range, and the amplitude of the attenuation can exceed 80% of the maximum value. Figure 16 shows the Von Mises stress plot under a Hanning-modulated seven-sinusoidal-cycle excitation signal with a center frequency of 580 Hz. As shown in Figure 16a, when the Lamb wave passes through the metamaterial-free region, the energy does not suffer a loss, and it can carry the energy to travel a long distance. In Figure 16b, when the incident Lamb wave propagates in the metamaterial, the energy is obviously effectively absorbed. The propagation of the Lamb wave is attenuated and blocked, and the inner region of the metamaterial is hardly affected.

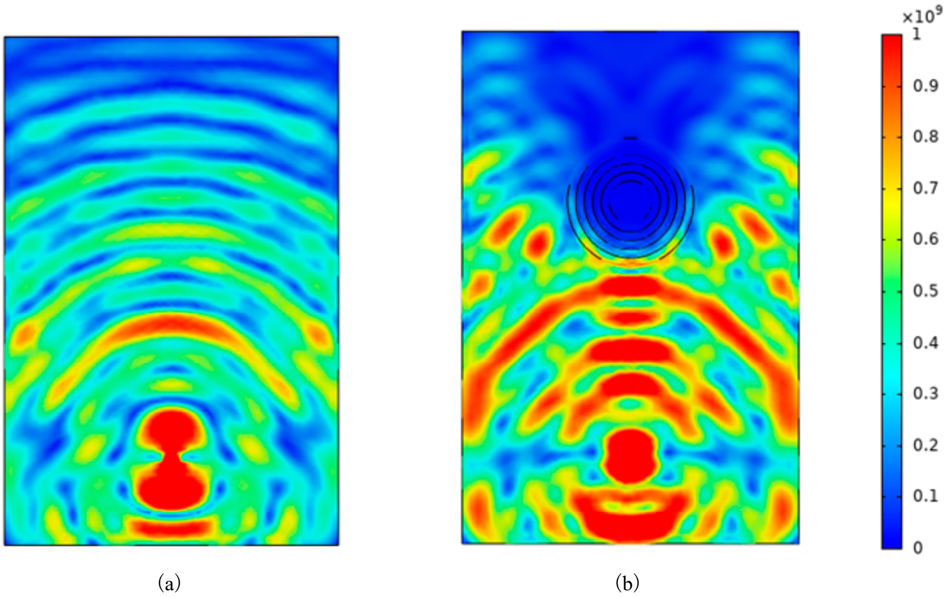

**Figure 16.** Von Mises stress distribution (**a**) without the metamaterial and (**b**) with the metamaterial.

## 5. Experimental Investigations on the Ultra-Low-Frequency Broadband Characteristics

To corroborate the theoretical results, this section is based on a five-period I-shaped radial metamaterial whose geometric parameters are as follows: the lattice constant $a = 20$ mm, the waist height $h = 20$ mm, the waist thickness $d = 12$ mm, and the average leg thickness $e = 4$ mm. Figure 17 shows the processing of the experimental sample. It is worth mentioning that the size parameters of the experimental sample are consistent with those in Figure 1c, to minimize the influence of the model on the experiment.

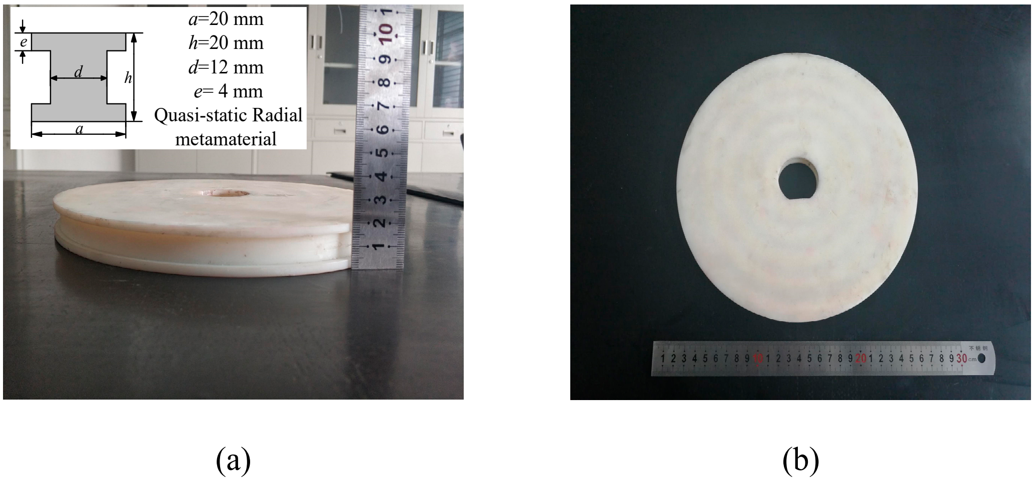

**Figure 17.** Experimental specimen of the I-shaped metamaterial plate: (**a**) side view and (**b**) front view.

In this paper, the radial metamaterial sample is adhered to the experimental bench to establish the surface constraint boundary conditions [36]. Subsequently, a quasi-static metamaterial is formed, as shown in Figure 18. Using the M + P dynamic analysis system, the vibration energy decay curve of the quasi-static experimental sample is collected, and the existence of the ultra-low-frequency broadband is verified. A pulsing hammer to make the sample vibrate is used. Subsequently, the vibration sensor installed in a specific position transmits the vibration displacement of the pulse hammer and the sample to the vibration analyzer. After the analysis and the calculation, the vibration energy attenuation curve of the tested sample is obtained.

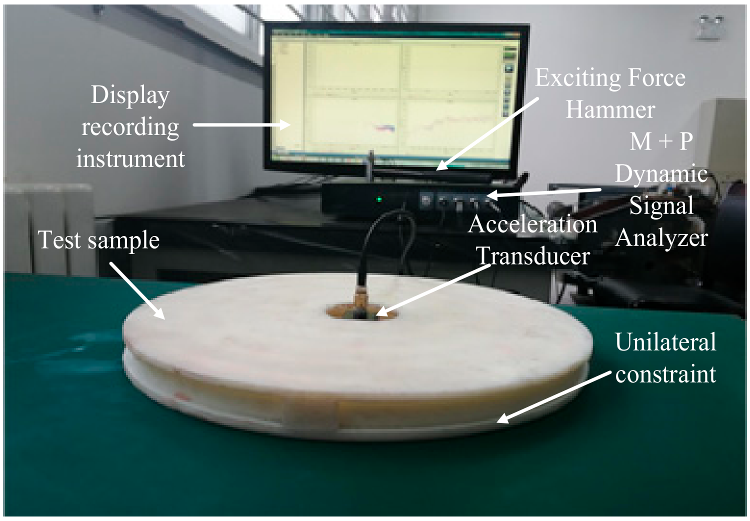

**Figure 18.** Experimental test system.

In this experiment, the transient excitation method of the hammer is adopted by using the vibration sensor to pick up multiple sets of data independently. To ensure the validity of the experimental data, the data are averaged. The experimental results are shown in Figure 19.

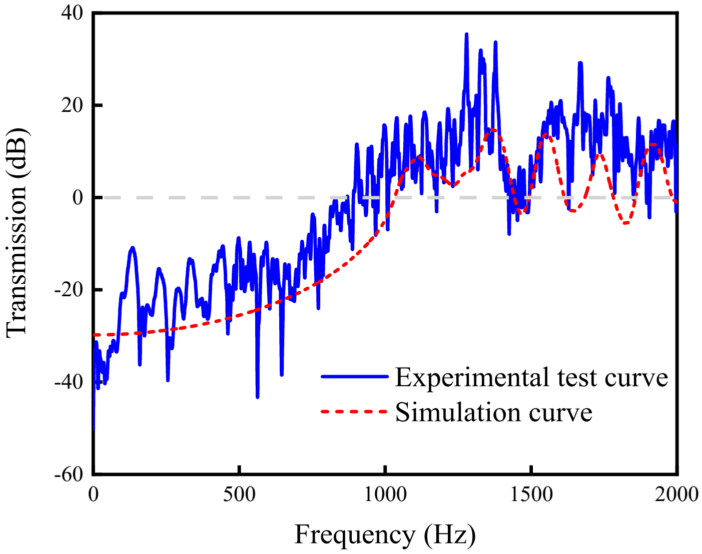

**Figure 19.** Specimen frequency response curve.

Figure 19 shows the experimental and simulated frequency response curves of the specimen. The results show that a large attenuation region appears at 0.1–1012 Hz. The initial frequency of the band gap is in good agreement with the experimental results, but there is a discrepancy between the cut-off frequencies of the simulation results and experimental results. The main reason for the discrepancy is that the fixed boundary conditions, as specified in the theoretical method, cannot be fully guaranteed on the installation method of the specimen in the vibration experiment. In the finite element model, the base surface is a fixed constraint boundary condition, but the installation method of the specimen in the experiments cannot completely guarantee the realization of the constraint boundary conditions of the base surface. In the experimental structure, the cut-off frequency is shifted to the low frequency because the existence of damping at the sensor connection dissipates the natural vibration energy of the system. Therefore, the cut-off frequency exhibits a certain error. Furthermore, the materials (epoxy) in the simulation are all linear elastic, homogeneous, and isotropic. However, they are not perfect ideal models for the experiments. Although there are some differences between the experimental results and the simulation results, they both indicate the existence of ultra-low-frequency broadband. The simulation results are, therefore, consistent with the experimental results.

## 6. Conclusions

We proposed and demonstrated an I-shaped REM and investigated the characteristics and changes of the quasi-static band gap. The ultra-low-frequency broadband mechanism was analyzed; the variation in the ultra-low-frequency broadband of the quasi-static I-shaped REMs was explored with the changes in the geometric parameters. Finally, the experimental sample based on the model was designed and prepared. The existence of an ultra-low-frequency broadband with an onset of close to 0 Hz in the structure was confirmed by using the stop-band and pass-band energy attenuation characteristics of the I-shaped REMs in different states.

The investigations show that the band gap properties of the I-shaped REMs were affected by the inherent vibration properties of their structures. The constraints were found to influence the intrinsic properties of the structure, thereby affecting the band gap characteristics of the structure. The quasi-static I-shaped radial metamaterial structure exhibited ultra-low-frequency broadband characteristics. It was found that the generation mechanism of the ultra-low-frequency broadband was the formation of the ultra-low-frequency band gap by fixed constraints, and the resonance frequency of the oscillator was the key factor to realize the ultra-broadband. The band gap gradually increased with the increase in the parameter $d/a$. The reason for this increase was that the metamaterial provided both equivalent stiffness and equivalent mass. The dynamic change in the equivalent stiffness $K_e$ with $d/a$ was the main reason for the change in the band gap. With the increase in the parameter $d/a$, the torsional stiffness of the structure increased, the torsional vibration was weakened, the radial vibration was strengthened, and the width of the band gap was gradually widened. The experimental results showed that the quasi-static metamaterial had a wide frequency band of 0.1–1012 Hz, which confirmed that the quasi-static I-shaped REM can generate ultra-low-frequency broadband.

In conclusion, a quasi-static I-shaped radial elastic metamaterial that exhibited ultra-low-frequency broadband was proposed and demonstrated. The research results have important practical significance for engineering fields such as seismic wave shielding and other ultra-low-frequency vibration reduction applications.

**Author Contributions:** Conceptualization, H.L.; Supervision, L.L.; Visualization, W.H.; Writing—original draft, Q.J. All authors have read and agreed to the published version of the manuscript.

**Funding:** This research was funded by the Natural Science Foundation of China (No. 51405368) and the Natural Science Foundation of China Shaanxi Province under grants (No. 2017JM5024).

**Institutional Review Board Statement:** Not applicable.

**Informed Consent Statement:** Not applicable.

**Data Availability Statement:** Not applicable.

**Conflicts of Interest:** The authors declare no conflict of interest.

## References

1. Sigalas, M.; Economou, E.N. Elastic and Acoustic Wave Band Structure. *J. Sound Vib.* **1992**, *158*, 377–382. [CrossRef]
2. Flores Parra, E.A.; Bergamini, A.; Van Damme, B.; Ermanni, P. Controllable Wave Propagation of Hybrid Dispersive Media with LC High-Pass and Band-Pass Networks. *Appl. Phys. Lett.* **2017**, *110*, 184103. [CrossRef]
3. Kushwaha, M.; Halevi, P.; Dobrzynski, L.; Djafari-Rouhani, B. Acoustic Band Structure of Periodic Elastic Composites. *Phys. Rev. Lett.* **1993**, *71*, 2022–2025. [CrossRef] [PubMed]
4. Goffaux, C.; Maseri, F.; Vasseur, J.O.; Djafari-Rouhani, B.; Lambin, P. Measurements and Calculations of the Sound Attenuation by a Phononic Band Gap Structure Suitable for an Insulating Partition Application. *Appl. Phys. Lett.* **2003**, *83*, 281–283. [CrossRef]

5. Yeh, J.Y.; Chen, L.W. Wave Propagations of a Periodic Sandwich Beam by FEM and the Transfer Matrix Method. *Compos. Struct.* **2006**, *73*, 53–60. [CrossRef]
6. Liu, Z.; Zhang, X.; Mao, Y.; Zhu, Y.Y.; Yang, Z.; Chan, C.T.; Sheng, P. Locally Resonant Sonic Materials. *Science* **2000**, *289*, 1734–1736. [CrossRef]
7. Jian, W.; Xiao-Chun, B.; Yong, X.; Ming-Xin, G.; Dian-Long, Y.; Ji-Hong, W. Low frequency band gaps and vibration reduction properties of a multi-frequency locally resonant phononic plate. *Acta Phys. Sin.* **2016**, *65*, 064602. [CrossRef]
8. Hussein, M.I.; Leamy, M.J.; Ruzzene, M. Dynamics of Phononic Materials and Structures: Historical Origins, Recent Progress, and Future Outlook. *Appl. Mech. Rev.* **2014**, *66*, 040802. [CrossRef]
9. Wu, J.; Ma, F.; Zhang, S.; Shen, L. Application of Acoustic Metamaterials in Low-frequency Vibration and Noise Reduction. *J. Mech. Eng.* **2016**, *52*, 68–78. [CrossRef]
10. Ma, G.; Sheng, P. Acoustic Metamaterials: From Local Resonances to Broad Horizons. *Sci. Adv.* **2016**, *2*, e1501595. [CrossRef] [PubMed]
11. Nouh, M.; Aldraihem, O.; Baz, A. Wave Propagation in Metamaterial Plates with Periodic Local Resonances. *J. Sound Vib.* **2015**, *341*, 53–73. [CrossRef]
12. Matlack, K.H.; Bauhofer, A.; Krödel, S.; Palermo, A.; Daraio, C. Composite 3D-Printed Meta-Structures for Low Frequency and Broadband Vibration Absorption. *Proc. Natl. Acad. Sci. USA* **2015**, *113*, 8386–8390. [CrossRef]
13. Ma, F.; Wu, J.H.; Huang, M.; Zhang, W.; Zhang, S. A Purely Flexible Lightweight Membrane-Type Acoustic Metamaterial. *J. Phys. D Appl. Phys.* **2015**, *48*, 175105. [CrossRef]
14. Badreddine Assouar, M.; Oudich, M. Enlargement of a Locally Resonant Sonic Band Gap by Using Double-Sides Stubbed Phononic Plates. *Appl. Phys. Lett.* **2012**, *100*, 123506. [CrossRef]
15. Krushynska, A.O.; Kouznetsova, V.G.; Geers, M.G.D. Towards Optimal Design of Locally Resonant Acoustic Metamaterials. *J. Mech. Phys. Solids* **2014**, *71*, 179–196. [CrossRef]
16. Gao, N.; Wu, J.H.; Yu, L. Research on Bandgaps in Two-Dimensional Phononic Crystal with Two Resonators. *Ultrasonics* **2015**, *56*, 287–293. [CrossRef]
17. Torrent, D.; Sánchez-Dehesa, J. Radial Wave Crystals: Radially Periodic Structures from Anisotropic Metamaterials for Engineering Acoustic or Electromagnetic Waves. *Phys. Rev. Lett.* **2009**, *103*, 064301. [CrossRef]
18. Zhu, X.; Liang, B.; Kan, W.; Zou, X.; Cheng, J. Acoustic Cloaking by a Superlens with Single-Negative Materials. *Phys. Rev. Lett.* **2011**, *106*, 014301. [CrossRef] [PubMed]
19. Torrent, D.; Sánchez-Dehesa, J. Acoustic Resonances in Two-Dimensional Radial Sonic Crystal Shells. *New J. Phys.* **2010**, *12*, 073034. [CrossRef]
20. Li, Y.; Zhou, Q.; Zhu, L.; Guo, K. Hybrid Radial Plate-Type Elastic Metamaterials for Lowering and Widening Acoustic Bandgaps. *Int. J. Mod. Phys. B* **2018**, *32*, 1850286. [CrossRef]
21. An, S.; Shu, H.; Liang, S.; Shi, X.; Zhao, L. Band Gap Characteristics of Radial Wave in a Two-Dimensional Cylindrical Shell with Radial and Circumferential Periodicities. *AIP Adv.* **2018**, *8*, 035110. [CrossRef]
22. Gao, N.; Hou, H.; Wu, J.H.; Cheng, B. Low Frequency Band Gaps below 10 Hz in Radial Flexible Elastic Metamaterial Plate. *J. Phys. D Appl. Phys.* **2016**, *49*, 435501. [CrossRef]
23. Shi, X.; Shu, H.; Zhu, J.; Wang, X.; Dong, L.; Zhao, L.; Liang, S.; Liu, R. Research on Wave Bandgaps in a Circular Plate of Radial Phononic Crystal. *Int. J. Mod. Phys. B* **2016**, *30*, 1650162. [CrossRef]
24. Gao, N.; Wu, J.H.; Guan, D. Research on the Large Band Gaps in Multilayer Radial Phononic Crystal Structure. *Mod. Phys. Lett. B* **2016**, *30*, 1650108. [CrossRef]
25. Ma, T.; Chen, T.; Wang, X.; Li, Y.; Wang, P. Band Structures of Bilayer Radial Phononic Crystal Plate with Crystal Gliding. *J. Appl. Phys.* **2014**, *116*, 104505. [CrossRef]
26. Li, Y.; Chen, T.; Wang, X.; Yu, K.; Chen, W. Propagation of Lamb Waves in One-Dimensional Radial Phononic Crystal Plates with Periodic Corrugations. *J. Appl. Phys.* **2014**, *115*, 054907. [CrossRef]
27. Gao, N.; Hou, H.; Xin, H. A Single and Double Slotting Radial Acoustic Metamaterial Plate. *Mod. Phys. Lett. B* **2017**, *31*, 1750128. [CrossRef]
28. Yao, S.; Zhou, X.; Hu, G. Investigation of the Negative-Mass Behaviors Occurring below a Cut-off Frequency. *New J. Phys.* **2010**, *12*, 103025. [CrossRef]
29. Craster, R.; Kaplunov, J.; Pichugin, A. High-Frequency Homogenization for Periodic Media. *R. Soc. Lond. Proc. Ser. A* **2010**, *466*, 2341–2362. [CrossRef]
30. Achaoui, Y.; Antonakakis, T.; Brûlé, S.; Craster, R.V.; Enoch, S.; Guenneau, S. Clamped Seismic Metamaterials: Ultra-Low Frequency Stop Bands. *New J. Phys.* **2017**, *19*, 063022. [CrossRef]
31. Oh, J.H.; Assouar, B. Quasi-Static Stop Band with Flexural Metamaterial Having Zero Rotational Stiffness. *Sci. Rep.* **2016**, *6*, 33410. [CrossRef] [PubMed]
32. Yu, K. *Research on the Bandgap Mechanism and Its Application Basis of Phononic Crystals with Slit Characteristic*; Xi'an Jiaotong University: Xi'an, China, 2017.
33. Achaoui, Y.; Khelif, A.; Benchabane, S.; Robert, L.; Laude, V. Experimental Observation of Locally-Resonant and Bragg Band Gaps for Surface Guided Waves in a Phononic Crystal of Pillars. *Phys. Rev. B* **2011**, *83*, 104201. [CrossRef]

34. Krushynska, A.O.; Kouznetsova, V.G.; Geers, M.G.D. Visco-Elastic Effects on Wave Dispersion in Three-Phase Acoustic Metamaterials. *J. Mech. Phys. Solids* **2016**, *96*, 29–47. [CrossRef]
35. Wen, X. *Sheng zi jing ti =: Phononic Crystals*; Di 1 ban.; Guo Fang Gong Ye Chu Ban She: Beijing, China, 2009; ISBN 978-7-118-06342-4.
36. Lefebvre, G.; Antonakakis, T.; Achaoui, Y.; Craster, R.V.; Guenneau, S.; Sebbah, P. Unveiling Extreme Anisotropy in Elastic Structured Media. *Phys. Rev. Lett.* **2017**, *118*, 254302. [CrossRef] [PubMed]